Gate-Tuning Hybrid Polaritons in Twisted α-MoO₃/Graphene Heterostructures

Zhou Zhou,[△] Renkang Song,[△] Junbo Xu,[△] Xiang Ni, Zijia Dang, Zhichen Zhao, Jiamin Quan, Siyu Dong, Weida Hu, Di Huang, Ke Chen,[*] Zhanshan Wang, Xinbin Cheng, Markus B. Raschke,[*] Andrea Alù,[*] and Tao Jiang[*]
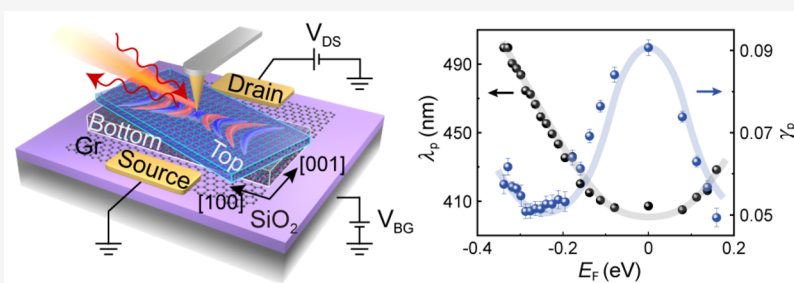
ACCESS | Metrics & More | Article Recommendations | SI Supporting Information

ABSTRACT: Modulating anisotropic phonon polaritons (PhPs) can open new avenues in infrared nanophotonics. Promising PhP dispersion engineering through polariton hybridization has been demonstrated by coupling gated graphene to single-layer α-MoO₃. However, the mechanism underlying the gate-dependent modulation of hybridization has remained elusive. Here, using IR nanospectroscopic imaging, we demonstrate active modulation of the optical response function, quantified in measurements of gate dependence of wavelength, amplitude, and dissipation rate of the hybrid plasmon−phonon polaritons (HPPPs) in both single-layer and twisted bilayer α-MoO₃/graphene heterostructures. Intriguingly, while graphene doping leads to a monotonic increase in HPPP wavelength, amplitude and dissipation rate show transition from an initially anticorrelated decrease to a correlated increase. We attribute this behavior to the intricate interplay of gate-dependent components of the HPPP complex momentum. Our results provide the foundation for active polariton control of integrated α-MoO₃ nanophotonics devices.

KEYWORDS: gate−tuning, hybrid plasmon−phonon polaritons, twisted α-MoO₃, dispersion, s-SNOM

PhPs are quasiparticles formed by the hybridization of light and optical phonons in polar crystals.[1,2] Their deeply subwavelength optical confinement and low loss, emerging in several polar crystals at infrared (IR) frequencies,[2,3] have been laying the foundation of a new paradigm for IR nanophotonic technologies. When the principal elements of the in-plane permittivity tensor show opposite signs, highly confined in-plane hyperbolic PhPs emerge, with signature hyperbolic-shaped iso-frequency contours (IFCs),[3,4] as demonstrated in the vdW materials α-MoO₃[5,6] and α-V₂O₅[7] as well as in polar crystals calcite[8,9] and beta-phase Ga₂O₃ (bGO).[10] In particular, PhPs in α-MoO₃ have demonstrated exciting opportunities for deeply subwavelength nanofocusing[11−13] and negative refraction.[14,15] Control of PhPs in α-MoO₃ through the modification of the dielectric environment,[16−21] chemical intercalation,[22−25] and isotope enrichment[26] has been achieved and recently extended through the formation of hybrid polaritons in twisted bilayer α-MoO₃[27−30] and a single-layer α-MoO₃/graphene heterostructure.[31−36] Particularly, gate tuning the resulting in-plane hybrid polaritons can give rise to active control of

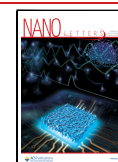topological transitions in the IFCs[35,36] and negative refraction.[31]

Despite the demonstration of active modulation of polariton hybridization mentioned above, there is still an open question regarding the underlying mechanism behind the gate-dependent behavior. Therefore, it is crucial to comprehensively analyze the modulated variation behaviors of the fundamental parameters of hybrid polaritons: wavelength (λ_p), amplitude (A_p), and dissipation rate (γ_p). In this article, using infrared scattering-type scanning near-field optical microscopy (IR s-SNOM), we demonstrate the active modulation of hybrid plasmon−phonon polaritons (HPPPs) in both single-layer and twisted bilayer α-MoO₃/graphene heterostructures. Most
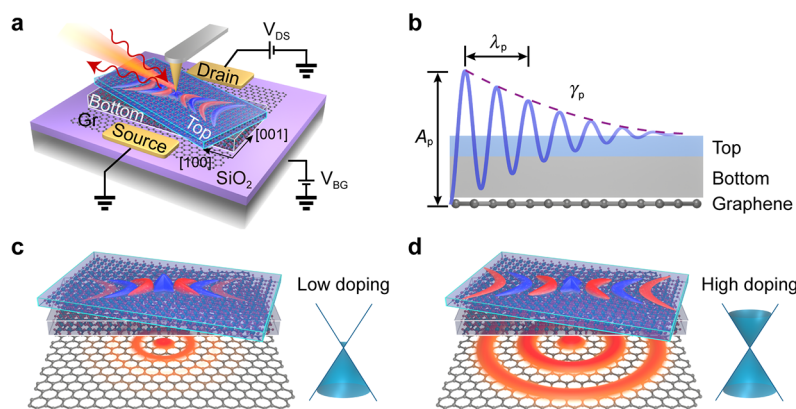
Figure 1. Illustration of gate-tuning hybrid plasmon−phonon polaritons in a twisted bilayer α-MoO$_3$/graphene heterostructure. (a) Schematic of IR s-SNOM measurement for the twisted bilayer α-MoO$_3$/graphene device, wherein an infrared 931 cm^{-1} laser beam was focused on a gold-coated atomic force microscopy (AFM) tip, and the backscattered light was collected to extract near-field signals. (b) Illustration of three key parameters of HPPPs: wavelength (λ_p), amplitude (A_p), and dissipation rate (γ_p) in twisted bilayer α-MoO$_3$/graphene heterostructures. (c,d) Illustration of coupling between α-MoO$_3$ phonon polaritons and graphene surface plasmon polaritons for (c) low and (d) high graphene doping.
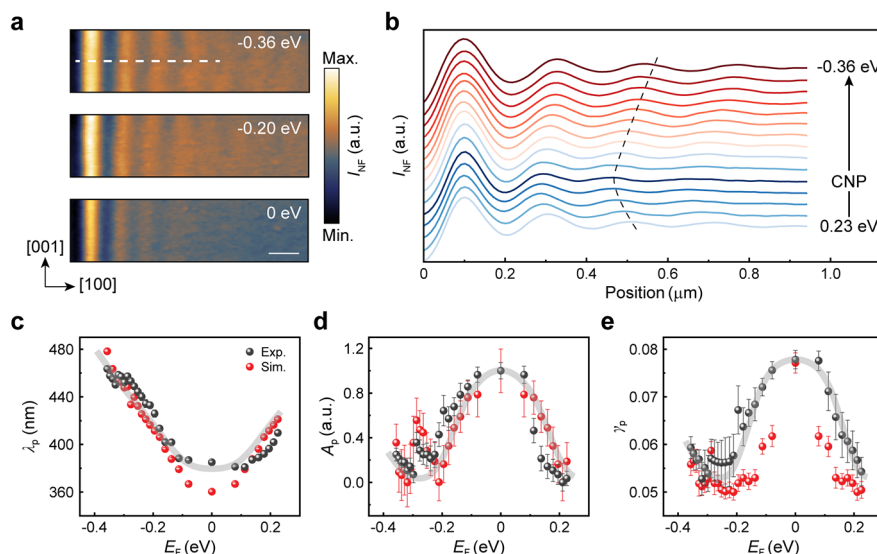

Figure 2. Gate-tuning hybrid plasmon−phonon polaritons in a single-layer α-MoO$_3$/graphene device. (a) Near-field images of the single-layer α-MoO$_3$/graphene heterostructure region with $E_F = -0.36$ (top panel), −0.20 (middle panel), and 0 eV (bottom panel). The thickness of α-MoO$_3$ is 140 nm. Scale bar: 200 nm. (b) IR s-SNOM line profiles extracted along the [100] crystal direction of α-MoO$_3$ (white dashed line in (a)) and averaged at different locations over 500 nm in the [001] crystal direction, as the back gate voltage V_g was swept from 70 V (corresponding to 0.23 eV, bottom line profile) to −70 V (corresponding to −0.36 eV, top line profile) in increments of 10 V. The graphene CNP occurs at 30 V. The black dashed curve indicates the variation trend of λ_p with E_F. (c−e) Dependence of (c) λ_p, (d) normalized A_p, and (e) γ_p on E_F, as fitted from experimental (black dots) and numerically simulated (red dots) line profiles of HPPPs. The error bars represent the 95% confidence intervals. Gray solid lines are guides for the eye.

notably, we unveil the underlying gate-dependent mechanism by probing the nanooptical response function, quantified in measurements of gate dependence of λ_p, A_p, and γ_p of HPPPs. Intriguingly, we observe a monotonic increase in λ_p and an initially anticorrelated decrease and then correlated increase of A_p and γ_p with the absolute value of graphene Fermi energy $|E_F|$. This behavior is attributed to the distinct dependencies of λ_p, A_p, and γ_p on the HPPP real and imaginary parts of the complex momentum. Our work systematically establishes nontrivial correlations of the key optical parameters of HPPPs with the E_F-dependent complex optical conductivity of graphene, forming the basis for active hybrid polariton control in integrated IR nanophotonic technologies.

To experimentally investigate the gate-tuning properties of HPPPs, we designed and fabricated two types of α-MoO$_3$/

graphene devices. For single-layer α-MoO$_3$/graphene devices, we dry transferred single-layer α-MoO$_3$ with 140 nm thickness on top of a monolayer graphene on a silicon substrate (with a 285 nm silica dielectric layer). For twisted bilayer α-MoO$_3$/graphene devices, the bottom and top α-MoO$_3$ layers, with thicknesses of 134 and 46 nm, respectively, were sequentially stacked on top of a monolayer graphene with a relative 47° twist angle between the [100] crystal direction of two α-MoO$_3$ layers (see Methods for details). We modified E_F by applying a gate voltage to the silicon substrate. The graphene charge neutral point (CNP) is determined by two independent methods: gate-dependent electronic transport measurements and third-harmonic generation (THG) intensity measurements, showing consistent results (see Supporting Information, section 1 for details).
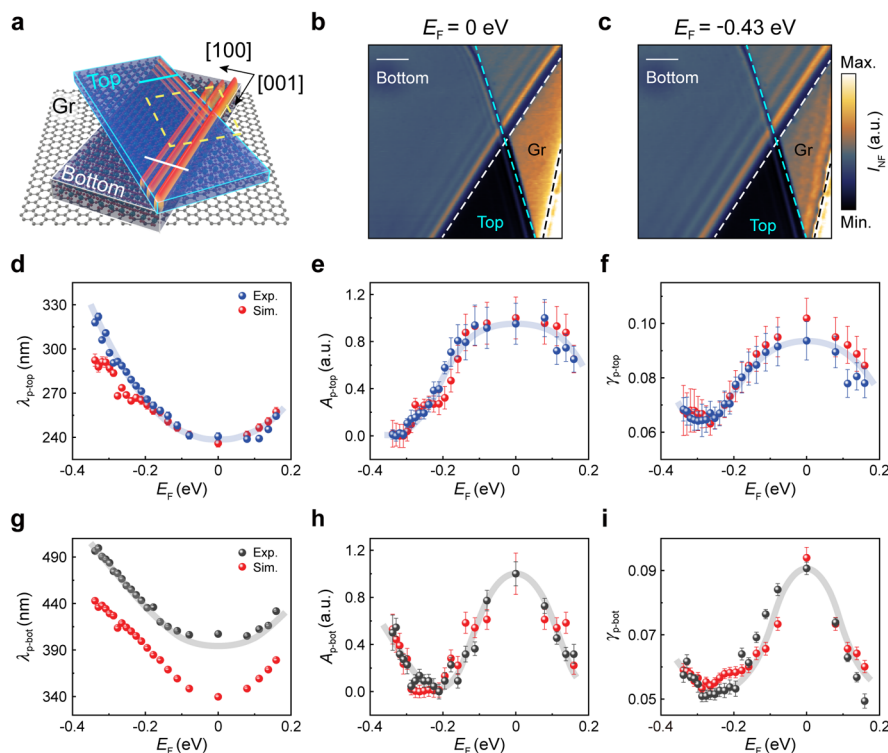
Figure 3. Gate-tuning hybrid plasmon−phonon polaritons in the twisted bilayer α-MoO₃/graphene device. (a) Schematic of the twisted bilayer α-MoO₃/graphene heterostructure. The bottom and top α-MoO₃ layers have thicknesses of 134 and 46 nm, respectively. The twist angle is 47°. The interference fringes along both the top and bottom α-MoO₃ layer edges can be detected in IR *s*-SNOM nanoimaging. (b,c) Near-field images of the twisted bilayer α-MoO₃/graphene device with (b) $E_F = 0$ eV and (c) $E_F = -0.43$ eV. The imaging area is marked by a yellow dashed square in (a). Cyan, white, and black dashed lines indicate the edges of the top and bottom α-MoO₃ layers and the gold electrode, respectively. Fringes in the graphene region in (c) are graphene SPPs, which are absent in (b) due to the significant damping at $E_F = 0$ eV. Scale bars: 500 nm. (d−i) Dependence of (d,g) λ_p, (e,h) normalized A_p, and (f,i) γ_p on E_F, extracted from fitting experimental (blue and black dots, Figure S11) and numerically simulated (red dots) line profiles of HPPPs along the [100] crystal direction of the (d−f) top (cyan solid line in (a)) and (g−i) bottom (white solid line in (a)) α-MoO₃ layers. The error bars represent the 95% confidence intervals. Blue and gray solid lines are guides for the eye.

IR *s*-SNOM HPPP nanoimaging was performed at the frequency of 931 cm⁻¹ with homodyne near-field detection, as illustrated in Figure 1a (see Methods for details). HPPPs are launched by a gold-coated tip, propagating and interfering with the reflected wave by the α-MoO₃ edge. From line profiles of the resulting interference fringes, we retrieve the λ_p, A_p, and γ_p of HPPPs, as shown in Figure 1b. Additionally, we conducted two-phase homodyne near-field detection on the twisted bilayer α-MoO₃/graphene device, showing consistent results with the homodyne measurements and providing further confirmation of the accuracy and validity of our experimental findings (see Supporting Information, section 5 for details).

In terms of numerical simulations, we used the finite-difference time-domain (FDTD) method to simulate the HPPP fringes as measured in experiments. The optical response of α-MoO₃ and graphene was modeled by a Lorentz oscillator and the Kubo formula, respectively. The real part of the out-of-plane electric field Re (E_z) of the HPPP waves was retrieved from the simulations (see Supporting Information, section 2 for details).

The gate tunability of the emerging HPPPs is illustrated in Figure 1c and d. The level of graphene E_F significantly modifies the dispersion and dissipation rate of the graphene surface plasmon polaritons (SPPs),[37−39] consequently influencing the dispersion of HPPPs in the twisted bilayer α-MoO₃/graphene heterostructure, for low (Figure 1c) and high (Figure 1d) doping levels.

We first characterized HPPPs in single-layer α-MoO₃/graphene devices as a reference. Figure 2a shows near-field images for three values of E_F, 0 eV (top), −0.20 eV (middle), and −0.36 eV (bottom), showcasing remarkable variations in λ_p, A_p, and γ_p of polariton interference fringes as a function of E_F. We then performed sweeps of back-gate voltage V_g from 70 to −70 V (E_F: from 0.23 to −0.36 eV) in increments of 5 V. Figure 2b shows the corresponding IR *s*-SNOM line profile of near-field images with 10 V increments of V_g (see Figure S6 for line profiles at other V_g values).

We fit the line profiles intensity I_{NF} of HPPPs using a model that accounts for geometric spread and interference between tip-launched and edge-reflected polariton waves (see Supporting Information, section 6 for more details)

$$I_{NF} = A_p \frac{e^{-2\pi\gamma_p/\lambda_p x}}{\sqrt{x}} \sin\left(2\pi \frac{x - x_c}{\lambda_p}\right) + B \frac{e^{-4\pi\gamma_p/\lambda_p x}}{x} + I_0,$$

$$A_p > 0, \lambda_p > 0, \gamma_p > 0, B > 0 \tag{1}$$

with physical fit parameters A_p, γ_p, λ_p, x_c, B, and I_0. Figure 2c shows the derived values of λ_p increasing monotonically with $|E_F|$. Correspondingly, A_p and γ_p, shown in Figure 2d and e, respectively, are correlated and initially decrease, yet then increase with increasing $|E_F|$, with a turning point at ∼0.2 eV. The experimental data for another device with a single-layer α-MoO₃ thickness of 175 nm are shown in Figure S14. We
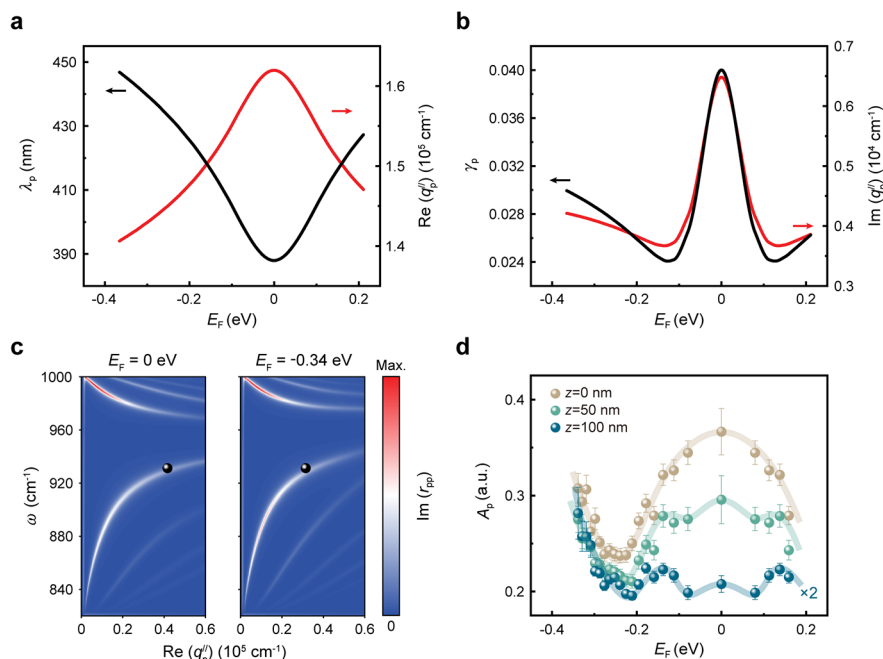
Figure 4. Gate-tuning mechanism of hybrid plasmon−phonon polaritons. (a,b) Theoretically calculated E_F dependence of λ_p, γ_p (black lines) and $\mathrm{Re}(q_p^{\parallel})$, $\mathrm{Im}(q_p^{\parallel})$ (red lines) for a twisted bilayer α-MoO$_3$/graphene heterostructure, which has the same α-MoO$_3$ thicknesses and twist angle as the device shown in Figure 3. The direction of the in-plane momentum $q_p^{\parallel}$ is along the [100] crystal direction of the bottom α-MoO$_3$ layer. (c) Calculated dispersion (color plots) of HPPPs in the twisted bilayer α-MoO$_3$/graphene heterostructure with $E_F = 0$ eV (left panel) and $E_F = -0.34$ eV (right panel). The direction of in-plane momentum $q_p^{\parallel}$ is along the [100] crystal direction of the top α-MoO$_3$ layer. The black dots represent experimental data extracted from Figure 3d. (d) Numerically simulated E_F dependence of A_p at heights of $z = 0$, 50, and 100 nm, indicated by brown, light green, and light blue dots, respectively. The error bars represent the 95% confidence intervals. Color solid lines are guides for the eye.

compare these experimental observations with numerical simulations of the near-field fringes (see Supporting Information, section 6 for more details). The derived values for λ_p, A_p, and γ_p, and predicted variations with E_F, are in good agreement with our experimental results.

Next, we performed corresponding experiments on the twisted bilayer α-MoO$_3$/graphene device, as shown in Figure 3. Figure 3b and c shows near-field images taken in the area marked by the yellow dashed square in Figure 3a, for $E_F = 0$ and -0.43 eV, respectively. In this area, two sets of polariton interference fringes are observed due to the interference between tip-launched polariton waves and their reflections from the edges of the top and bottom α-MoO$_3$ layers.

Applying the same analysis as above, we retrieve two sets of λ_p, A_p, and γ_p as a function of E_F along the [100] crystal direction of the top and bottom α-MoO$_3$ layer edges, as shown in Figure 3d−i (see Figure S5 for additional data for a similar device). Analogous to the single-layer α-MoO$_3$/graphene device, both λ_{p-top} (Figure 3d) and λ_{p-bot} (Figure 3g) increase monotonically with $|E_F|$. Simultaneously, the amplitude (A_{p-top} in Figure 3e and A_{p-bot} in Figure 3h) and dissipation rate (γ_{p-top} in Figure 3f and γ_{p-bot} in Figure 3i) exhibit an inflection point at $|E_F| \sim 0.2$ eV. We attribute the slight differences in the variation of A_{p-top} (γ_{p-top}) and A_{p-bot} (γ_{p-bot}) to the difference in the real part of the HPPP complex in-plane momentum along the edges of the top and bottom α-MoO$_3$ layers. We also performed simulations analogous to the single-layer α-MoO$_3$/graphene device, which also shows good agreement with experiments. Additional simulations exploring various twist angles and α-MoO$_3$ thicknesses are shown in Figures S7−9.

The mechanism underlying the demonstrated gate-dependence behavior of HPPPs can be explained based on the

variation of the complex momentum with E_F. The quantities λ_p, A_p, and γ_p are associated with the in-plane $q_p^{\parallel}$ and out-of-plane q_z momentum components through:[40,41]

$$\lambda_p = 1/\mathrm{Re}(q_p^{\parallel}) \tag{2}$$

$$\gamma_p = \mathrm{Im}(q_p^{\parallel})/\mathrm{Re}(q_p^{\parallel}) \tag{3}$$

$$A_p = A_0 \cdot e^{-iq_z z} \tag{4}$$

where A_0 is the HPPP amplitude at the surface of α-MoO$_3$, and z is the height above the α-MoO$_3$ surface where the near-field signal is detected. Note that we consider only $q_p^{\parallel}$ along the [100] crystal direction of α-MoO$_3$, consistent with our experiments. The dependence of $\mathrm{Re}(q_p^{\parallel})$ and $\mathrm{Im}(q_p^{\parallel})$ with E_F, as predicted from the theory (see Supporting Information, section 4), is shown in Figure 4a and b, respectively. Our theory indeed confirms the observed dependence of λ_p with $|E_F|$ (Figure 4a). Furthermore, due to the interplay between $1/\mathrm{Re}(q_p^{\parallel})$ and $\mathrm{Im}(q_p^{\parallel})$ in determining the damping rate, following eq 3, γ_p initially decreases with $|E_F|$, reaching an inflection point at ~0.2 eV, and then increases (Figure 4b).

The derived variations of λ_p and γ_p are in good agreement with the experimental and numerical simulation results shown in the previous section. Despite the dependence on both $\mathrm{Im}(q_p^{\parallel})$ and $\mathrm{Re}(q_p^{\parallel})$, due to the weaker variation of $\mathrm{Re}(q_p^{\parallel})$ with E_F (Figure 4a), γ_p (E_F) follows the variation of $\mathrm{Im}(q_p^{\parallel})(E_F)$ to first order. For illustration, Figure 4c shows the underlying calculated dispersion of the HPPPs (see Supporting Information, section 3) for two selected values of E_F (see Figures S15−18 for other values of E_F). With increasing $|E_F|$, $\mathrm{Re}(q_p^{\parallel})$ becomes smaller at a given frequency, and the

experimental data (black dots in Figure 4c) are in good agreement with the calculations.

At last, apart from the expected general decrease of A_p with distance z, A_p varies nontrivially with E_F and differently as the distance from the sample varies (Figure 4d). Based on the dependence of the evanescent q_z with E_F (Figure S12), for larger distances z, the term $e^{-iq_z z}$ in eq 4 dominates the behavior of A_p, giving rise to an overall increase of A_p with $|E_F|$. However, when z is close to 0, A_p scales similarly to A_0, which is affected by the propagation length of HPPPs, showing the same inflection point as γ_p. In contrast, γ_p is solely associated with the in-plane complex momentum $q_p^{\parallel}$. Therefore, the variation of γ_p remains independent of z, as shown in Figure S13b. We attribute the slight deviation in inflection points between theoretically calculated and experimental trends to the inaccuracies introduced by the infinite conductor model used in our calculations. It is worth noting that while the twist angle and the thickness of α-MoO_3 would influence the absolute values of $\mathrm{Re}(q_p^{\parallel})$ and $\mathrm{Im}(q_p^{\parallel})$ our observations regarding the gate-tuning behaviors of HPPPs remain consistent and broadly applicable across different twist angles and α-MoO_3 thicknesses, as detailed in the Supporting Information, section 7.

In summary, we investigated the gate dependence of HPPPs stemming from the coupling between PhPs in α-MoO_3 and SPPs in graphene. By modulating the graphene E_F, we demonstrated gate tunability of the optical response in IR s-SNOM measurements, retrieving the dependence of three key HPPP parameters, i.e., wavelength, amplitude, and dissipation rate, in heterostructure devices composed of single-layer and twisted bilayer α-MoO_3/graphene. Combined with numerical simulations and theoretical calculations, we showed how gate tunability is fundamentally controlled by the E_F-dependent optical conductivity of monolayer graphene. Our work highlights how λ_p, A_p, and γ_p can be tailored by the real and imaginary parts of the momentum associated with the gate-tunable polaritons. Their complex dependence originates from the intricate interplay of gate-dependent in-plane and out-of-plane components of the HPPP complex momentum. The elucidation of the gate-dependent mechanism of hybrid polaritons, along with its successful implementation in twisted bilayer α-MoO_3/graphene devices, establishes the foundation for harnessing the full potential of gate tuning of hybrid polariton systems for nanophotonic devices in the infrared regime, yielding reprogrammable polaritonics and real-time control over nanoscale light routing and confinement. Coupled with localized quantum emitters, the demonstrated platform may modulate in real-time light−matter coupling and emission features, paving the way for a range of opportunities for nanophotonics.

METHODS

Device Fabrication and Characterization. Monolayer graphene was mechanically exfoliated from graphite crystals (Shanghai Onway Technology Co.,Ltd.) onto a plasma-treated (SUNJUNE PLASMA VP-R3) SiO_2 (285 nm)/Si substrate. α-MoO_3 flakes were exfoliated from bulk materials (SixCarbon technology, Shenzhen) onto polydimethylsiloxane (PDMS). The desired thickness of α-MoO_3 was checked and selected under optical microscopy before being stacked onto graphene via all-dry transfer methods to prevent any chemical contamination. To fabricate twisted bilayer α-MoO_3/graphene devices, top and bottom α-MoO_3 flakes with selected thicknesses were separately exfoliated onto PDMS and dry transferred onto monolayer graphene sequentially, with the desired twist angle achieved using a micromanipulator. Drain and source electrodes (50 nm Au/5 nm Cr) were evaporated onto the graphene through a prepatterned shadow mask using thermal deposition. The sample was then mounted on a compact chip carrier, with all electrodes wire-bonded to it for electrical gating and doping.

IR s-SNOM Measurements. Near-field images were obtained using a commercially available IR s-SNOM system (Bruker nanoIR3s) operating in tapping mode AFM. An IR beam with a frequency of 931 cm^{-1} was generated by a CO_2 laser (Access Laser, L4SL-13CO2) and focused on the apex of a gold-coated AFM tip (160AC-GG, OPUS) with tapping frequency $\Omega \approx 270$ kHz. The backscattered light from the tip was collected with an off-axis parabolic mirror and directed to a HgCdTe (MCT) photodetector to extract the near-field signal from the device. Detected signals were demodulated at the second harmonic to suppress the background.

Electric Transport and THG Measurements. The back-gate voltage was applied using a SourceMeter (Keithley, 2450), and the graphene resistance was recorded by a lock-in amplifier (Ametek, 7270). For THG measurement, a mid-IR femtosecond laser beam (Carmina, APE GmbH) with a center wavelength at 2850 nm (0.44 eV) was focused on the α-MoO_3/graphene heterostructure through a 0.5 NA reflective objective (Thorlabs, LMM40X-P01). The back-reflected THG signal was gathered and guided to a spectrometer (HRS-500MS, Teledyne Princeton Instruments). In-situ recording of the gate-dependent THG signal was performed while sweeping the back-gate voltage. Throughout the electric transport and THG measurements, devices were maintained in a dry air environment to avoid the effects of atmospheric moisture on the devices.

■ ASSOCIATED CONTENT

Ⓢ Supporting Information

The Supporting Information is available free of charge at https://pubs.acs.org/doi/10.1021/acs.nanolett.3c03769.

> Determination of graphene CNP and E_F, numerical simulations, calculation of polariton dispersion, theoretical calculation of relation between HPPP complex momentum and graphene conductivity, two-phase homodyne near-field detection of the twisted bilayer α-MoO_3/graphene device, derivation of fitting equations, gate-tuning behavior of HPPPs in twisted bilayer α-MoO_3/graphene across varying twist angles and α-MoO_3 thicknesses, gate tuning of topological transition in twisted bilayer α-MoO_3/graphene heterostructures (PDF)

■ AUTHOR INFORMATION

Corresponding Authors

Ke Chen − *Center for the Physics of Low-Dimensional Materials, School of Physics and Electronics, School of Future Technology, Henan University, Kaifeng 475004, China;* ⓘ orcid.org/0000-0003-2384-8437; Email: kchen@henu.edu.cn

Markus B. Raschke − *Department of Physics and JILA, University of Colorado, Boulder, Colorado 80309, United States;* ⓘ orcid.org/0000-0003-2822-851X; Email: markus.raschke@colorado.edu

Andrea Alù − *Photonics Initiative, Advanced Science Research Center, City University of New York, New York, New York 10031, United States; Physics Program, Graduate Center, City University of New York, New York, New York 10026, United States;* ⊙ orcid.org/0000-0002-4297-5274; Email: aalu@gc.cuny.edu

Tao Jiang − *MOE Key Laboratory of Advanced Micro-Structured Materials, Shanghai Frontiers Science Center of Digital Optics, Institute of Precision Optical Engineering, and School of Physics Science and Engineering, Tongji University, Shanghai 200092, China;* ⊙ orcid.org/0000-0001-8656-1738; Email: tjiang@tongji.edu.cn

Authors

Zhou Zhou − *MOE Key Laboratory of Advanced Micro-Structured Materials, Shanghai Frontiers Science Center of Digital Optics, Institute of Precision Optical Engineering, and School of Physics Science and Engineering, Tongji University, Shanghai 200092, China; Shanghai Institute of Intelligent Science and Technology, Tongji University, Shanghai 200092, China*

Renkang Song − *MOE Key Laboratory of Advanced Micro-Structured Materials, Shanghai Frontiers Science Center of Digital Optics, Institute of Precision Optical Engineering, and School of Physics Science and Engineering, Tongji University, Shanghai 200092, China*

Junbo Xu − *MOE Key Laboratory of Advanced Micro-Structured Materials, Shanghai Frontiers Science Center of Digital Optics, Institute of Precision Optical Engineering, and School of Physics Science and Engineering, Tongji University, Shanghai 200092, China*

Xiang Ni − *Photonics Initiative, Advanced Science Research Center, City University of New York, New York, New York 10031, United States; School of Physics, Central South University, Changsha, Hunan 410083, China*

Zijia Dang − *Center for the Physics of Low-Dimensional Materials, School of Physics and Electronics, School of Future Technology, Henan University, Kaifeng 475004, China*

Zhichen Zhao − *MOE Key Laboratory of Advanced Micro-Structured Materials, Shanghai Frontiers Science Center of Digital Optics, Institute of Precision Optical Engineering, and School of Physics Science and Engineering, Tongji University, Shanghai 200092, China*

Jiamin Quan − *Photonics Initiative, Advanced Science Research Center, City University of New York, New York, New York 10031, United States; Physics Program, Graduate Center, City University of New York, New York, New York 10026, United States*

Siyu Dong − *MOE Key Laboratory of Advanced Micro-Structured Materials, Shanghai Frontiers Science Center of Digital Optics, Institute of Precision Optical Engineering, and School of Physics Science and Engineering, Tongji University, Shanghai 200092, China*

Weida Hu − *State Key Laboratory of Infrared Physics, Shanghai Institute of Technical Physics, Chinese Academy of Sciences, Shanghai 200083, China;* ⊙ orcid.org/0000-0001-5278-8969

Di Huang − *MOE Key Laboratory of Advanced Micro-Structured Materials, Shanghai Frontiers Science Center of Digital Optics, Institute of Precision Optical Engineering, and School of Physics Science and Engineering, Tongji University, Shanghai 200092, China;* ⊙ orcid.org/0000-0003-3698-5158

Zhanshan Wang − *MOE Key Laboratory of Advanced Micro-Structured Materials, Shanghai Frontiers Science Center of Digital Optics, Institute of Precision Optical Engineering, and School of Physics Science and Engineering, Tongji University, Shanghai 200092, China; Shanghai Institute of Intelligent Science and Technology, Tongji University, Shanghai 200092, China;* ⊙ orcid.org/0000-0002-2161-6934

Xinbin Cheng − *MOE Key Laboratory of Advanced Micro-Structured Materials, Shanghai Frontiers Science Center of Digital Optics, Institute of Precision Optical Engineering, and School of Physics Science and Engineering, Tongji University, Shanghai 200092, China; Shanghai Institute of Intelligent Science and Technology, Tongji University, Shanghai 200092, China;* ⊙ orcid.org/0000-0002-3855-483X

Complete contact information is available at:
https://pubs.acs.org/10.1021/acs.nanolett.3c03769

Author Contributions

△Z.Z., R.S., and J.X. contributed equally to this work; T.J. conceived and designed the experiments; Z.Z. conducted the near-field and electric transport measurements with guidance from T.J. and M.B.R.; A.A. suggested the model and supervised the development of the theory; R.S. fabricated devices with the help of S.D. and support from W.H., X.C., and Z.W.; R.S. performed the THG measurements; J.X. and Z.D. performed the simulations with guidance from X.N. and K.C.; J.X. and X.N. contributed to the theory with guidance from A.A.; Z.Z. and J.X. contributed to the data fitting and analysis with guidance from T.J. and D.H.; Z.Z. wrote the manuscript with the help of all authors. All authors discussed and interpreted the results.

Notes

The authors declare no competing financial interest.

■ ACKNOWLEDGMENTS

■ REFERENCES

(1) Renger, J.; Grafström, S.; Eng, L. M.; Hillenbrand, R. Resonant light scattering by near-field-induced phonon polaritons. *Phys. Rev. B* **2005**, *71*, No. 075410.

(2) Caldwell, J. D.; Lindsay, L.; Giannini, V.; Vurgaftman, I.; Reinecke, T. L.; Maier, S. A.; Glembocki, O. J. Low-loss, infrared and terahertz nanophotonics using surface phonon polaritons. *Nanophotonics* **2015**, *4*, 44−68.

(3) Hu, G.; Shen, J.; Qiu, C.-W.; Alù, A.; Dai, S. Phonon Polaritons and Hyperbolic Response in van der Waals Materials. *Advanced Optical Materials* **2020**, *8*, No. 1901393.

(4) Lee, D.; So, S.; Hu, G.; Kim, M.; Badloe, T.; Cho, H.; Kim, J.; Kim, H.; Qiu, C.-W.; Rho, J. Hyperbolic metamaterials: fusing artificial structures to natural 2D materials. *eLight* **2022**, *2*, 1.

(5) Ma, W.; et al. In-plane anisotropic and ultra-low-loss polaritons in a natural van der Waals crystal. *Nature* **2018**, *562*, 557−562.

(6) Zheng, Z.; Xu, N.; Oscurato, S. L.; Tamagnone, M.; Sun, F.; Jiang, Y.; Ke, Y.; Chen, J.; Huang, W.; Wilson, W. L.; Ambrosio, A.; Deng, S.; Chen, H. A mid-infrared biaxial hyperbolic van der Waals crystal. *Science Advances* **2019**, *5*, No. eaav8690.

(7) Taboada-Gutiérrez, J.; et al. Broad spectral tuning of ultra-low-loss polaritons in a van der Waals crystal by intercalation. *Nat. Mater.* **2020**, *19*, 964−968.

(8) Ma, W.; Hu, G.; Hu, D.; Chen, R.; Sun, T.; Zhang, X.; Dai, Q.; Zeng, Y.; Alù, A.; Qiu, C.-W.; Li, P. Ghost hyperbolic surface polaritons in bulk anisotropic crystals. *Nature* **2021**, *596*, 362−366.

(9) Hu, C.; Sun, T.; Zeng, Y.; Ma, W.; Dai, Z.; Yang, X.; Zhang, X.; Li, P. Source-configured symmetry-broken hyperbolic polaritons. *eLight* **2023**, *3*, 14.

(10) Passler, N. C.; Ni, X.; Hu, G.; Matson, J. R.; Carini, G.; Wolf, M.; Schubert, M.; Alù, A.; Caldwell, J. D.; Folland, T. G.; Paarmann, A. Hyperbolic shear polaritons in low-symmetry crystals. *Nature* **2022**, *602*, 595−600.

(11) Qu, Y.; et al. Tunable Planar Focusing Based on Hyperbolic Phonon Polaritons in α-MoO₃. *Adv. Mater.* **2022**, *34*, No. 2105590.

(12) Zheng, Z.; Jiang, J.; Xu, N.; Wang, X.; Huang, W.; Ke, Y.; Zhang, S.; Chen, H.; Deng, S. Controlling and Focusing In-Plane Hyperbolic Phonon Polaritons in α-MoO₃ with a Curved Plasmonic Antenna. *Adv. Mater.* **2022**, *34*, No. 2104164.

(13) Martín-Sánchez, J.; Duan, J.; Taboada-Gutiérrez, J.; Álvarez Pérez, G.; Voronin, K. V.; Prieto, I.; Ma, W.; Bao, Q.; Volkov, V. S.; Hillenbrand, R.; Nikitin, A. Y.; Alonso-González, P. Focusing of in-plane hyperbolic polaritons in van der Waals crystals with tailored infrared nanoantennas. *Science Advances* **2021**, *7*, No. eabj0127.

(14) Sternbach, A. J.; Moore, S. L.; Rikhter, A.; Zhang, S.; Jing, R.; Shao, Y.; Kim, B. S. Y.; Xu, S.; Liu, S.; Edgar, J. H.; Rubio, A.; Dean, C.; Hone, J.; Fogler, M. M.; Basov, D. N. Negative refraction in hyperbolic hetero-bicrystals. *Science* **2023**, *379*, 555−557.

(15) Zhang, T.; Zheng, C.; Chen, Z. N.; Qiu, C.-W. Negative Reflection and Negative Refraction in Biaxial van der Waals Materials. *Nano Lett.* **2022**, *22*, 5607−5614.

(16) Zheng, Z.; Sun, F.; Xu, N.; Huang, W.; Chen, X.; Ke, Y.; Zhan, R.; Chen, H.; Deng, S. Tunable Hyperbolic Phonon Polaritons in a Suspended van der Waals α-MoO₃ with Gradient Gaps. *Advanced Optical Materials* **2022**, *10*, No. 2102057.

(17) Schwartz, J. J.; Le, S. T.; Krylyuk, S.; Richter, C. A.; Davydov, A. V.; Centrone, A. Substrate-mediated hyperbolic phonon polaritons in MoO₃. *Nanophotonics* **2021**, *10*, 1517−1527.

(18) Yang, J.; Tang, J.; Ghasemian, M. B.; Mayyas, M.; Yu, Q. V.; Li, L. H.; Kalantar-Zadeh, K. High-Q Phonon-polaritons in Spatially Confined Freestanding α-MoO₃. *ACS Photonics* **2022**, *9*, 905−913.

(19) Shen, J.; Zheng, Z.; Dinh, T.; Wang, C.; Chen, M.; Chen, P.; Ma, Q.; Jarillo-Herrero, P.; Kang, L.; Dai, S. Hyperbolic phonon polaritons with positive and negative phase velocities in suspended α-MoO₃. *Appl. Phys. Lett.* **2022**, *120*, No. 113101.

(20) Zhang, Q.; Ou, Q.; Hu, G.; Liu, J.; Dai, Z.; Fuhrer, M. S.; Bao, Q.; Qiu, C.-W. Hybridized Hyperbolic Surface Phonon Polaritons at α-MoO₃ and Polar Dielectric Interfaces. *Nano Lett.* **2021**, *21*, 3112−3119.

(21) Matveeva, O. G.; Tresguerres-Mata, A. I. F.; Kirtaev, R. V.; Voronin, K. V.; Taboada-Gutiérrez, J.; Lanza, C.; Duan, J.; Martín-Sánchez, J.; Volkov, V. S.; Alonso-González, P.; Nikitin, A. Y. Twist-tunable polaritonic nanoresonators in a van der Waals crystal. *npj 2D Mater. Appl.* **2023**, *7*, 31.

(22) Wu, Y.; Ou, Q.; Yin, Y.; Li, Y.; Ma, W.; Yu, W.; Liu, G.; Cui, X.; Bao, X.; Duan, J.; et al. Chemical switching of low-loss phonon polaritons in α-MoO₃ by hydrogen intercalation. *Nat. Commun.* **2020**, *11*, 2646.

(23) Zheng, Z.; Chen, J.; Wang, Y.; Wang, X.; Chen, X.; Liu, P.; Xu, J.; Xie, W.; Chen, H.; Deng, S.; Xu, N. Highly Confined and Tunable Hyperbolic Phonon Polaritons in Van Der Waals Semiconducting Transition Metal Oxides. *Adv. Mater.* **2018**, *30*, No. 1705318.

(24) Wu, Y.; Ou, Q.; Dong, S.; Hu, G.; Si, G.; Dai, Z.; Qiu, C. W.; Fuhrer, M. S.; Mokkapati, S.; Bao, Q. Efficient and Tunable Reflection of Phonon Polaritons at Built-In Intercalation Interfaces. *Adv. Mater.* **2021**, *33*, No. 2008070.

(25) Zhang, Y.-N.; Tang, Y.; Qi, L.; Feng, Y.; Li, M.; An, J.; Wang, L.; Zhu, H.; Li, B.; Li, D.; Li, S. Tailoring the Phonon Polaritons in α-MoO₃ via Proton Irradiation. *Advanced Optical Materials* **2023**, *11*, No. 2300180.

(26) Zhao, Y.; Chen, J.; Xue, M.; Chen, R.; Jia, S.; Chen, J.; Bao, L.; Gao, H.-J.; Chen, J. Ultralow-Loss Phonon Polaritons in the Isotope-Enriched α-MoO₃. *Nano Lett.* **2022**, *22*, 10208−10215.

(27) Hu, G.; Ou, Q.; Si, G.; Wu, Y.; Wu, J.; Dai, Z.; Krasnok, A.; Mazor, Y.; Zhang, Q.; Bao, Q.; Qiu, C.-W.; Alù, A. Topological polaritons and photonic magic angles in twisted α-MoO₃ bilayers. *Nature* **2020**, *582*, 209−213.

(28) Chen, M.; Lin, X.; Dinh, T. H.; Zheng, Z.; Shen, J.; Ma, Q.; Chen, H.; Jarillo-Herrero, P.; Dai, S. Configurable phonon polaritons in twisted α-MoO₃. *Nat. Mater.* **2020**, *19*, 1307−1311.

(29) Zheng, Z.; Sun, F.; Huang, W.; Jiang, J.; Zhan, R.; Ke, Y.; Chen, H.; Deng, S. Phonon Polaritons in Twisted Double-Layers of Hyperbolic van der Waals Crystals. *Nano Lett.* **2020**, *20*, 5301−5308.

(30) Duan, J.; Capote-Robayna, N.; Taboada-Gutiérrez, J.; Álvarez Pérez, G.; Prieto, I.; Martín-Sánchez, J.; Nikitin, A. Y.; Alonso-González, P. Twisted Nano-Optics: Manipulating Light at the Nanoscale with Twisted Phonon Polaritonic Slabs. *Nano Lett.* **2020**, *20*, 5323−5329.

(31) Hu, H.; Chen, N.; Teng, H.; Yu, R.; Xue, M.; Chen, K.; Xiao, Y.; Qu, Y.; Hu, D.; Chen, J.; Sun, Z.; Li, P.; de Abajo, F. J. G.; Dai, Q. Gate-tunable negative refraction of mid-infrared polaritons. *Science* **2023**, *379*, 558−561.

(32) Hu, H.; et al. Doping-driven topological polaritons in graphene/α-MoO₃ heterostructures. *Nat. Nanotechnol.* **2022**, *17*, 940−946.

(33) Ruta, F. L.; Kim, B. S. Y.; Sun, Z.; Rizzo, D. J.; McLeod, A. S.; Rajendran, A.; Liu, S.; Millis, A. J.; Hone, J. C.; Basov, D. N. Surface plasmons induce topological transition in graphene/α-MoO₃ heterostructures. *Nat. Commun.* **2022**, *13*, 3719.

(34) Zeng, Y.; Ou, Q.; Liu, L.; Zheng, C.; Wang, Z.; Gong, Y.; Liang, X.; Zhang, Y.; Hu, G.; Yang, Z.; Qiu, C.-W.; Bao, Q.; Chen, H.; Dai, Z. Tailoring Topological Transitions of Anisotropic Polaritons by Interface Engineering in Biaxial Crystals. *Nano Lett.* **2022**, *22*, 4260−4268.

(35) Bapat, A.; Dixit, S.; Gupta, Y.; Low, T.; Kumar, A. Gate tunable light−matter interaction in natural biaxial hyperbolic van der Waals heterostructures. *Nanophotonics* **2022**, *11*, 2329−2340.

(36) Álvarez Pérez, G.; González-Morán, A.; Capote-Robayna, N.; Voronin, K. V.; Duan, J.; Volkov, V. S.; Alonso-González, P.; Nikitin, A. Y. Active Tuning of Highly Anisotropic Phonon Polaritons in Van der Waals Crystal Slabs by Gated Graphene. *ACS Photonics* **2022**, *9*, 383−390.

(37) Fei, Z.; Rodin, A. S.; Andreev, G. O.; Bao, W.; McLeod, A. S.; Wagner, M.; Zhang, L. M.; Zhao, Z.; Thiemens, M.; Dominguez, G.; Fogler, M. M.; Neto, A. H. C.; Lau, C. N.; Keilmann, F.; Basov, D. N. Gate-tuning of graphene plasmons revealed by infrared nano-imaging. *Nature* **2012**, *487*, 82−85.

(38) Chen, J.; Badioli, M.; Alonso-González, P.; Thongrattanasiri, S.; Huth, F.; Osmond, J.; Spasenović, M.; Centeno, A.; Pesquera, A.; Godignon, P.; Zurutuza Elorza, A.; Camara, N.; de Abajo, F. J. G.; Hillenbrand, R.; Koppens, F. H. L. Optical nano-imaging of gate-tunable graphene plasmons. *Nature* **2012**, *487*, 77−81.

(39) In, C.; Kim, U. J.; Choi, H. Two-dimensional Dirac plasmon-polaritons in graphene, 3D topological insulator and hybrid systems. *Light: Science & Applications* **2022**, *11*, 313.

(40) Basov, D. N.; Fogler, M. M.; de Abajo, F. J. G. Polaritons in van der Waals materials. *Science* **2016**, *354*, No. aag1992.

(41) Low, T.; Chaves, A.; Caldwell, J. D.; Kumar, A.; Fang, N. X.; Avouris, P.; Heinz, T. F.; Guinea, F.; Martin-Moreno, L.; Koppens, F. Polaritons in layered two-dimensional materials. *Nat. Mater.* **2017**, *16*, 182−194.